

MCR-91-1340  
Contract NAS8-36431

Phase III  
Final Report      September 1991

---

# Intelligent Robotic Systems Study (IRSS)

(NASA-CR-184261) INTELLIGENT ROBOTIC  
SYSTEMS STUDY (IRSS), PHASE 3 Final Report  
(Martin Marietta Space Systems) 36 p

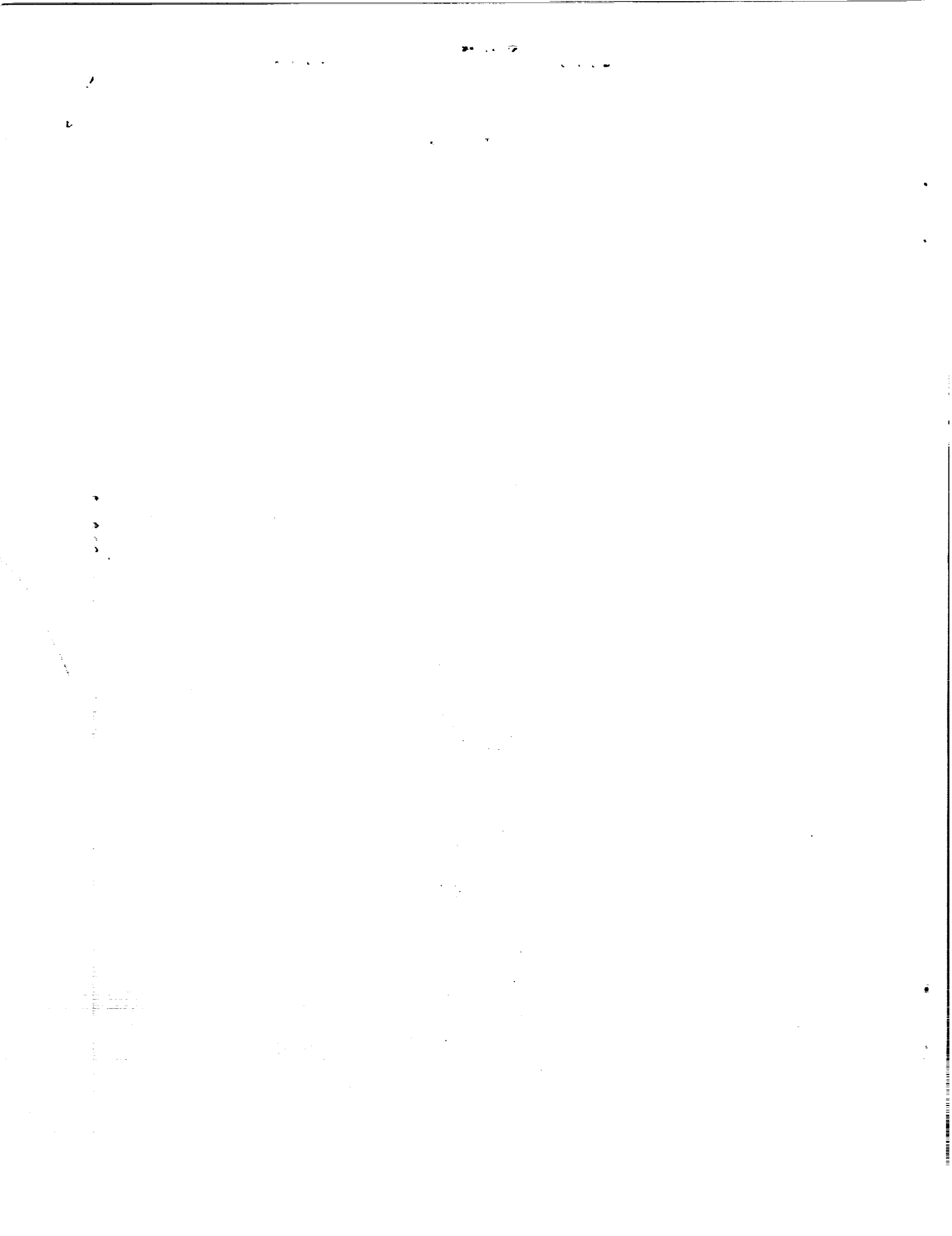
N92-14671

CSSL 09B

Unclas

G3/63 0053188

**MARTIN MARIETTA**



MCR-91-1340  
Contract NAS8-36431

Phase III  
Final Report

September 1991

---

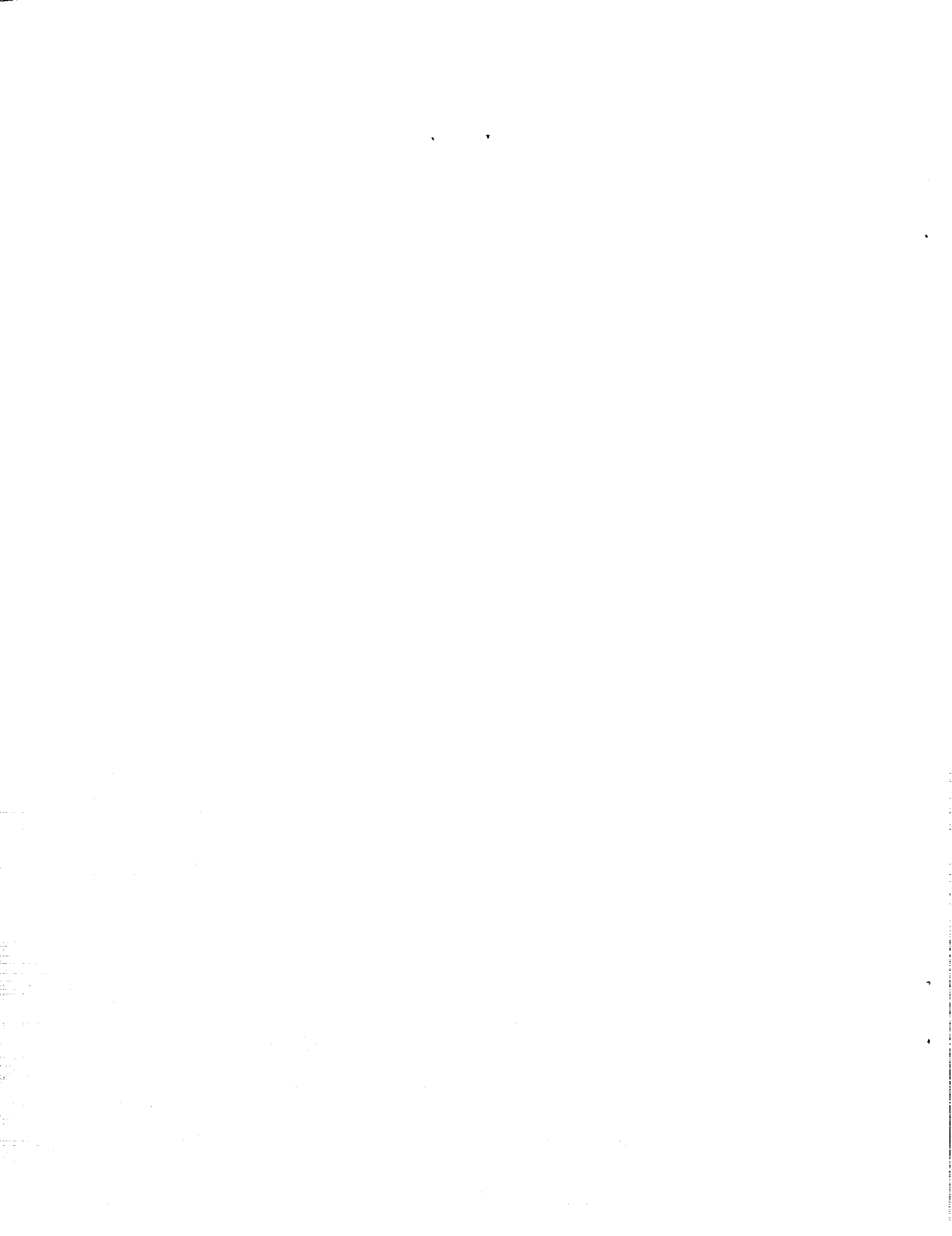
**INTELLIGENT ROBOTIC  
SYSTEMS STUDY  
(IRSS)**

**MARTIN MARIETTA  
ASTRONAUTICS GROUP**  
P.O. Box 179  
Denver, Colorado 80201



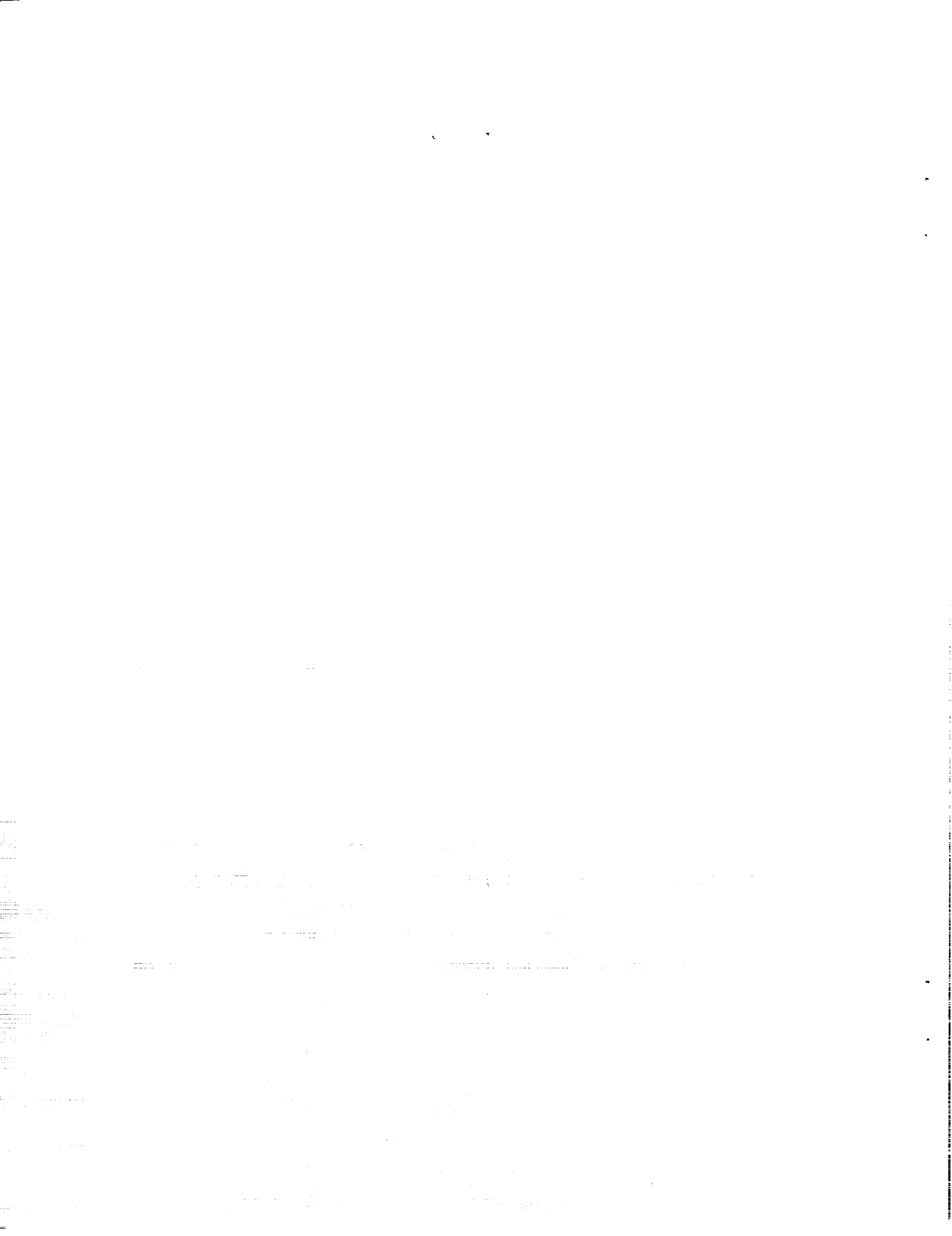
# Contents

<b>1</b>	<b>Introduction</b>	<b>1</b>
<b>2</b>	<b>Simulation Model</b>	<b>3</b>
2.1	Structural Model . . . . .	3
2.2	Manipulator Control Models . . . . .	5
2.2.1	Joint Position Control . . . . .	5
2.2.2	Endpoint Force Control . . . . .	5
2.3	Simulation and Analysis Tools . . . . .	6
<b>3</b>	<b>Analysis and Results</b>	<b>9</b>
3.1	Open-Loop Analysis . . . . .	9
3.2	Initial Closed-loop Analysis . . . . .	10
3.3	Effects of Stabilizer Stiffness and Controller Bandwidths . . . . .	12
3.4	Residual Vibration Reduction Using Preshaping Filters for Free-space Maneuvers . . . . .	14
3.5	ORU Extraction Simulations . . . . .	20
<b>4</b>	<b>Conclusions and Future Work</b>	<b>26</b>
<b>A</b>	<b>Constrained Dynamics Equations for Multi-link Planar Model</b>	<b>28</b>



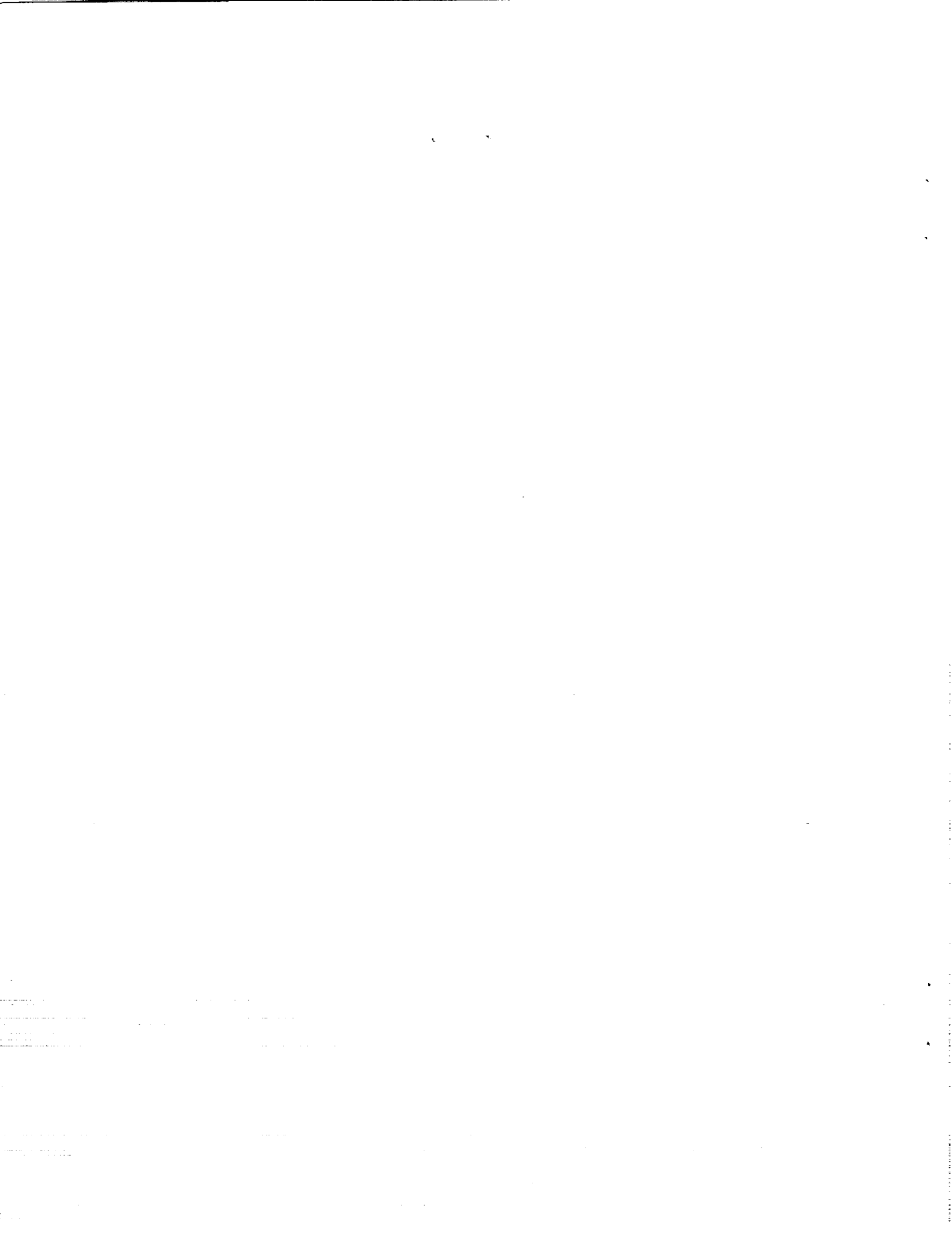
## List of Figures

1	Schematic of a planar FTS DTF-2 configuration . . . . .	1
2	Block diagram of the manipulator joint controllers. . . . .	6
3	Block diagram of the endpoint force controller. . . . .	6
4	MATRIXx/System-Build diagram illustrating TREETOPS interface. . . . .	7
5	The geometric configuration chosen for an ORU replace task. . . . .	10
6	Open and closed loop transfer functions for the nominal system . . . . .	11
7	System response for the nominal configuration . . . . .	13
8	Frequency and damping of the stabilizer mode as a function of stabilizer and attach-point stiffness . . . . .	14
9	Frequency and damping of stabilizer mode versus controller bandwidth . . . . .	15
10	System response using an improved stabilizer design . . . . .	16
11	Block diagram showing the use of command shaping filters. . . . .	16
12	Shaping of cartesian trajectory command with a four-impulse sequence. . . . .	17
13	System response using command shaping filter to reduce residual vibrations . . . . .	18
14	System response using shaping filter with 20% error. . . . .	19
15	Endpoint force control with and without joint rate feedback . . . . .	21
16	Simulation of 10 lb endpoint force control and ORU release from envi- ronment. . . . .	22
17	Simulation of 25 lb endpoint force control and ORU release from envi- ronment . . . . .	23
18	Simulation of 50 lb endpoint force control and ORU release from envi- ronment . . . . .	24
19	Comparison of cartesian responses for the two ORU extraction methods . . . . .	24
20	Comparison of nominal and improved stabilizer designs for a 50 lb ex- traction force . . . . .	25
21	FTS manipulator stabilized by flexible RMS manipulator . . . . .	27
22	Endpoint Inertial Forces and Torques . . . . .	30



## List of Tables

1	Worksite Stiffness Estimations . . . . .	4
2	FTS ASPS Stiffness Requirements . . . . .	4
3	Mass properties for the FTS DTF-2 model . . . . .	4
4	Open and closed loop system eigen analysis . . . . .	9
5	Comparison of responses for the four freespace simulations . . . . .	20
6	Comparison of endpoint settling times for ORU extraction simulations.	23



# 1 Introduction

This phase of the Intelligent Robotic Systems Study (IRSS) examines some basic dynamics and control issues for a space manipulator attached to its worksite through a compliant base. One example of this scenario is depicted in Fig. 1 which is a simplified, planar representation of the Flight Telerobotic Servicer (FTS) Development Test Flight 2 (DTF-2) experiment. The system consists of four major components: 1) dual FTS arms to perform dextrous tasks, 2) the main body to house power and electronics, 3) an Attachment Stabilization and Positioning Subsystem (ASPS) to provide coarse positioning and stabilization of the arms, and 4) the Worksite Attachment Mechanism (WAM) which anchors the system to its worksite, such as a Space Station truss node or Shuttle bay platform.

During a task, such as handling an ORU (Orbital Replacement Unit) payload, the manipulator degrees-of-freedom are actively controlled while the output brakes of the ASPS are locked for a given configuration of its joint angles. Because of joint flexibility in the ASPS output brakes and the WAM, moving a payload may induce undesired oscillations at these uncontrolled degrees of freedom. If the dominant vibration mode has a low frequency and is lightly damped, the residual vibrations at the end of a maneuver

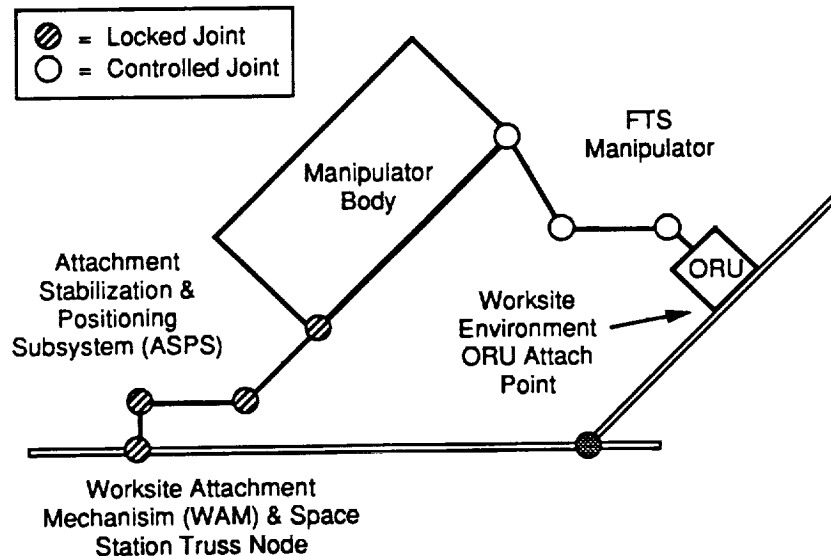


Figure 1: Schematic of a planar FTS DTF-2 configuration

could incur excessive settling times to the required control position accuracies. Another issue to consider is the arm/worksites dynamics interaction. For example, when one arm is pushing against the environment (ORU insertion) or extracting an ORU at the worksite location, what are the transient dynamic effects? How are the stability of the position (or impedance) control loops affected by the elastic base? During an extraction task when an ORU is suddenly released from its fixture, could the payload impact the worksite because of the body/stabilizer motion?

Another scenario of base compliance is the case of an FTS manipulator attached to the end-effector of a shuttle RMS or a space station MRMS. After coarse positioning is done, the RMS brakes are locked into position. The ASPS is either retracted or attached to the worksite. In this configuration, one arm is again pushing against, or pulling at a given area of the worksite. The same issues discussed above apply as well.

In this initial study, we limit our analysis to the DTF-2 scenario. The goal of this preliminary study is to understand the basic interaction dynamics between the arm, the positioner/stabilizer, and the worksite. Thus, to simplify the analysis, we consider a planar model consisting of a *single* FTS arm with the ASPS attached to a stationary worksite. Section 2 describes the dynamics and controls simulation model. To emphasize traceability to a realistic system, we have used as much as possible the currently defined properties of the DTF-2 system. Section 3 presents analysis and simulation results. After showing open-loop analysis and the potential for degraded closed-loop performance, we examine and demonstrate means for improvement. Section 4 summarizes conclusions and suggests future work, including possible hardware testbed experiments to complement and enhance the analysis reported here.

## 2 Simulation Model

In this section, we describe a simplified model of the FTS DTF-2 structure, the FTS manipulator control algorithm, all modelling assumptions, and the CAD software tools used for dynamics formulation, frequency-domain analysis and time-domain simulations.

### 2.1 Structural Model

A simplified planar model of the FTS DTF-2 structure is used throughout the analysis. Referring back to Fig. 1, the FTS arm and ASPS are modelled to include only the shoulder pitch, elbow pitch, and wrist pitch degrees-of-freedom. The attach-point is considered a single degree-of-freedom. With the exception of *joint* compliance at the ASPS and attach-point degrees-of-freedom, each member of the structure is assumed rigid (i.e., no *distributed* elasticity of the links or body). This results in a 7-DOF model.

Each joint of the ASPS and attach-point is modelled as a hinge with torsional stiffness,  $K_{jnt}$ . For the attach-point, the equivalent spring stiffness represents the series combination of rotational stiffnesses for the worksite attachment mechanism and the worksite itself. Table 1 summarizes estimated stiffness data for a variety of worksite attachment locations as given in [1]. As can be seen from the table, a space station truss node with rotational stiffness of 40,000 *ft-lb/radian* represents the most compliant environment. At this time, stiffness estimates are not yet available for the WAM; however, its stiffness is expected to be greater than that of a truss node. Thus, as a worst-case scenario,  $K_{att} = 40,000$  *ft-lb/radian* was chosen as the nominal value for the equivalent attach-point stiffness. Table 2 shows estimated stiffness requirements for the stabilizer/positioner [2]. Based on this data,  $K_{jnt} = 200,000$  *ft-lb/radian* was chosen as the nominal stiffness value for each ASPS joint.<sup>1</sup> Depending on the damping mechanism in the ASPS output brakes, the dynamic behavior of the FTS/stabilizer system could vary greatly from lightly damped (material damping) to moderately damped; however, little data is yet available. Assuming a worst-case scenario, a damping coefficient of 0.01 is assumed at each uncontrolled joint.

Table 3 summarizes the system mass properties used for the dynamic model. Except for some component mass estimates and initial dimensions, mass properties for the FTS body structure are not yet available; thus, we have done rough estimates to get center-of-mass (COM) locations and moment-of-inertia calculations. For the analysis in Section 3, a 25 *lb* ORU payload is assumed throughout; in the table, the ORU mass properties are included in the manipulator wrist  $M_W$ . With the exception of the manipulator body ( $M_B$ ) data, values in this table were provided by FTS personnel, and represent the most current DTF-2 system specifications available.

---

<sup>1</sup>Throughout the analysis, it is assumed that the three ASPS joint stiffnesses are always equal.

Attach-Point Location	Worksite Stiffness	
	Translation (lb/ft)	Torsion (ft-lb/rad)
Shuttle Bay *	100,000	100,000
Truss Node **	300,000	40,000
SIA Platform **	NA	45,000
ON Platform *	100,000	100,000

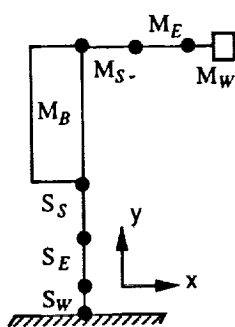
\* Estimate of worksite interface stiffness - no structural data available

\*\* Stiffness based on limited analysis of structure

Table 1: Worksite Stiffness Estimations

Joint	Minimum Stiffness			Minimum Braked Stiffness (ft-lb/rad)
	Torsion (ft-lb/rad)	Translation (lb/ft)	Bending (ft-lb/rad)	
Shoulder Roll	2,000	500,000	500,000	200,000
Shoulder Roll	2,000	500,000	500,000	200,000
Elbow Roll	2,000	500,000	500,000	200,000
Wrist Roll	2,000	500,000	500,000	200,000
Wrist Roll	2,000	500,000	500,000	200,000

Table 2: FTS ASPS Stiffness Requirements



Body	Mass (slug)	COM Inertia (slug-ft <sup>2</sup> )	COM Location		Length (ft)
			X (ft)	Y (ft)	
S <sub>W</sub>	0.6126	0.1481	0	0.3417	0.7500
S <sub>E</sub>	1.4367	0.6070	0	0.9675	1.8167
S <sub>S</sub>	1.1308	0.3216	0	0.8767	1.8167
M <sub>B</sub>	27.2600	50.8800	-0.7500	3.0000	4.6500
M <sub>S</sub>	1.4367	0.6070	0.9675	0	1.8167
M <sub>E</sub>	1.1308	0.3216	0.8767	0	1.8167
M <sub>W</sub>	3.0278	1.2276	1.0426	0	—

Table 3: Mass properties for the FTS DTF-2 model

## 2.2 Manipulator Control Models

Each FTS manipulator joint is driven by a brushless DC motor with a harmonic drive reduction transmission and is powered by a current-controlled PWM amplifier. Harmonic drive transmissions are characterized by a significant amount of nonlinear joint compliance and coulomb friction. Analog torque control loops are employed to directly control the output torque, making the actuator behave as a direct drive with very low friction. Laboratory tests have demonstrated that the torque control loops significantly stiffen the drive train and essentially cancel coulomb friction. Furthermore, in closed-loop, the actuator exhibits a flat, linear response to about 100 Hz, which is well beyond the position control bandwidth. As a result, no actuator dynamics are included in the simulation model. In the next section, simulation results are presented for two scenarios: 1) manipulation of a payload in freespace, and 2) extraction of a constrained ORU. Described below, the first scenario employs a joint position control law, while the second uses a simple endpoint force controller. For this initial study, endpoint impedance control schemes were not investigated. The controllers discussed below were implemented as a discrete system with a 100 Hz sampling rate.

### 2.2.1 Joint Position Control

Each joint position control loop consists of a proportional-derivative (PD) control law that is adjusted to provide a nominal 1 Hz bandwidth with a critically damped second-order response. In the system model, the individual joint control loops are inertially coupled by a non-diagonally dominant system inertia matrix. The coupling effect increases with load mass resulting in a full manipulator inertia matrix. This joint-to-joint coupling suggests the use of a simplified computed torque approach that uses a time-varying manipulator inertia matrix (a function of the elbow, and wrist joint angles) to cancel the controlled joint inertial coupling. This technique allows the use of an independent, uncoupled joint control loop design. <sup>2</sup> Figure 2 shows a block diagram of the joint position control loops.

### 2.2.2 Endpoint Force Control

For the case of an ORU extraction, it was assumed that the ORU could be rigidly grasped by the FTS wrist and that the ORU would remain rigidly attached to the environment. To remove the payload, endpoint force control was used to apply a specified extraction force normal to the payload's worksite fixture. The end-effector force/torque sensor is used for this mode.

Figure 3 shows a block diagram of the endpoint force controller which consists of

---

<sup>2</sup>Throughout the analysis, bandwidth and damping of the three position control loops are assumed identical

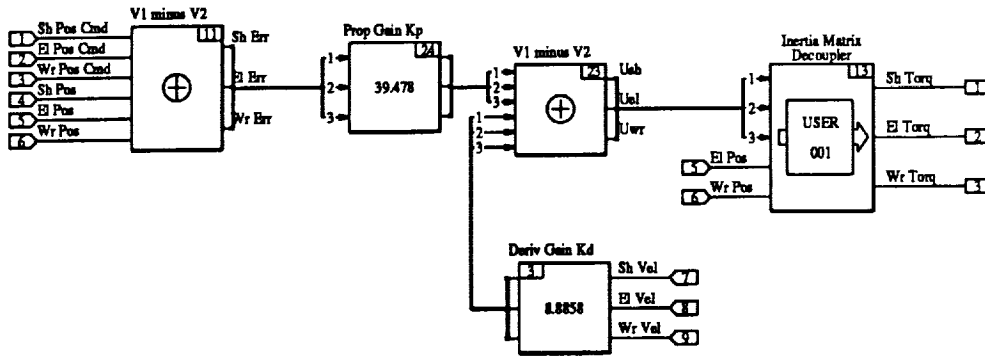


Figure 2: Block diagram of the manipulator joint position control loops with inertia matrix decoupling.

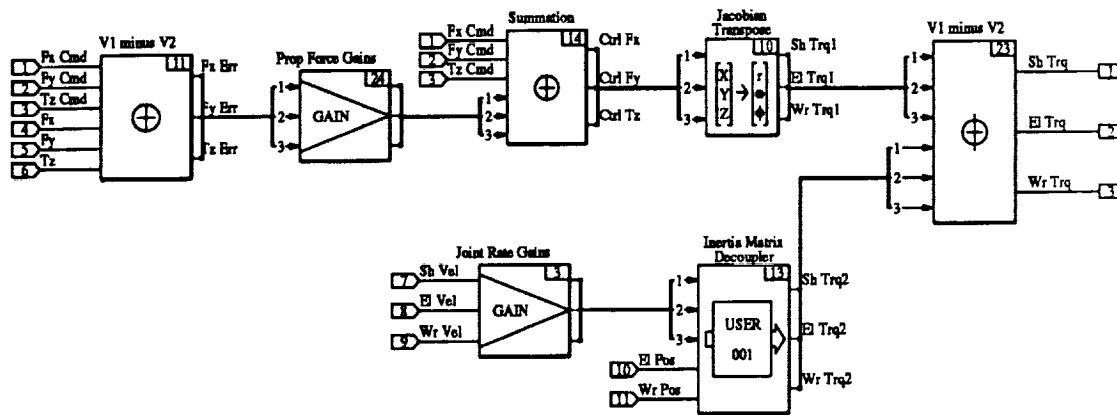


Figure 3: Block diagram of the endpoint force controller.

two basic feedback loops. In the outer loop, endpoint force/torque errors (given in cartesian space) are scaled by uncoupled proportional gains. The resulting cartesian control forces are then multiplied by the arm's Jacobian transpose to yield control commands in the manipulator's joint space. As with the inertia decoupling scheme, the Jacobian transformation assumes the 3-DOF manipulator is attached to a stationary base, thus ignoring motion of the stabilizer and FTS body. To improve damping characteristics of the force control, the inner loop was added and consists of proportional joint rate feedback. As with the position control loops described above, the inertia matrix decoupler is used here also.

### 2.3 Simulation and Analysis Tools

The software tools used in the simulation and analysis performed for this study include: TREETOPS, MATRIXx [7], and a multi-link planar simulation developed in-

house. TREETOPS is a software package which produces a time history simulation of multi-body systems consisting of rigid and/or flexible links connected in a tree topology. The dynamics equations are based on Kane's formulation and Lagrange's multiplier method. The code was initially developed by Honeywell and is currently being extended by DYNACS Engineering Inc., under contract to NASA Marshall Space Flight Center.

TREETOPS was originally intended as a modelling and simulation tool with some limited control system simulation modules. Under a Martin Marietta subcontract to the MATRIXx vendor, an interface was created to combine the advanced dynamics simulation capabilities of TREETOPS with the control system design and analysis tools of MATRIXx/System-Build. This interface allows the user to define a complex dynamical system using the TREETOPS set-up program, and then perform simulations, linearizations, and other analyses in MATRIXx. Figure 4 shows a sample System-Build block diagram used to simulate closed-loop control of the FTS DTF-2 system. Here, the TREETOPS block is used to model the manipulator/body/stabilizer dynamics.

The combined TREETOPS/MATRIXx tool was used to simulate the freespace, unconstrained configuration of the FTS DTF-2. For the case of constrained motion, it was discovered that the version of TREETOPS (Version 5.0) did not properly compute constraint forces and torques needed to simulate a force/torque sensor at the end-effector. Plans for 1991 include obtaining the most current TREETOPS version and updating the MATRIXx interface for it as well. Until then however, for the needs of this study software was developed to simulate the dynamics of a planar multi-link system with endpoint constraints and force/torque sensing. Appendix A summarizes the constrained dynamics equations used in the code. Because this multi-link program was inherently planar and due to its less complex nature, it was found to be on the order of twenty times faster than TREETOPS/MATRIXx for the FTS DTF-2 simulation. As does TREETOPS, the multi-link planar program employs a recursive method of Kane's dynamics to develop

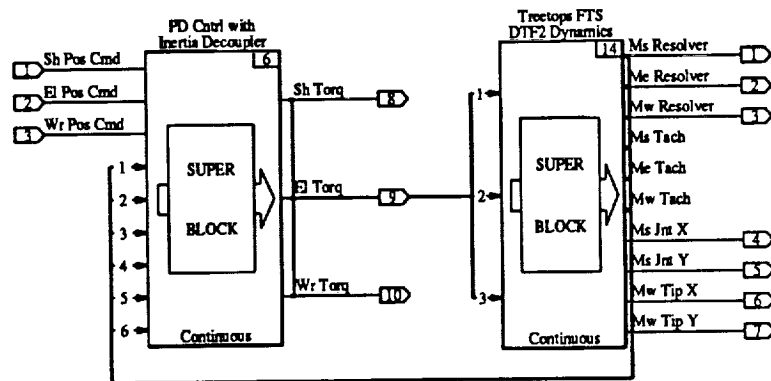


Figure 4: MATRIXx/System-Build diagram illustrating TREETOPS interface.

the unconstrained equations of motion [8] and uses Lagrange multipliers to determine the endpoint forces and torques [9]. It is implemented in the form of FORTRAN subroutines linked with MATRIXx and reads an input file at the beginning of a simulation to specify the link configuration and other parameters. Section 3.4 contains force control simulation results using the planar multi-link program.

### 3 Analysis and Results

We begin with an open-loop frequency analysis to obtain the basic characteristics of the flexibly stabilized manipulator system, and progress to the closed-loop system maneuvering a payload in freespace. It will be shown that for the nominal parameters of position control bandwidth and stabilizer/attach-point stiffnesses, the system is dominated by an uncontrolled, lightly damped, low frequency vibration mode which severely degrades tip position control performance. We then examine ways to alter the system dynamics for improved closed-loop performance, but at the expense of using stiffer components and/or reducing the position control bandwidth. Another alternative is explored which makes use of feed-forward filters to shape the reference commands in a way to reduce residual vibrations. Finally, we look at the transient responses when performing an ORU extraction task.

#### 3.1 Open-Loop Analysis

First we present an eigen analysis for the system with stabilizer joints braked, no manipulator control, and the nominal ASPS joint and attach point stiffnesses ( $K_{jnt} = 200,000$  and  $K_{att} = 40,000 \text{ ft-lb/rad}$ ). The geometric configuration is shown in Fig. 5. Shown in Figure 6 are the magnitude gain plots of the colocated transfer functions from joint torque to joint position for the three manipulator degrees-of-freedom. From this we see the system is characterized by alternating pairs of lightly damped and closely spaced zeros and poles. Four zero-pole pairs exist, one per each DOF of the stabilizer and attach-point, and range from  $0.74 \text{ Hz}$  to  $74 \text{ Hz}$  (see Table 4). These gain plots can be used to estimate the degree of coupling between each arm joint and the system modes. For instance, the first system mode shows the most gain in the elbow transfer function, indicating that excitation of the this mode would be seen mostly in the elbow response.

Clearly the 7-DOF system is kinematically nonlinear, and as such, the system modes will be configuration dependent. To illustrate, the eigenanalysis was repeated for six other arbitrary poses; the primary system mode ranged from  $0.62 \text{ Hz}$  to  $0.80 \text{ Hz}$ . Although

Flexible Mode #	Open-Loop System		Closed-Loop System	
	Frequency (Hz)	Damping Ratio	Frequency (Hz)	Damping Ratio
1	0.74	< .01	0.64	.03
2	9.6	.01	9.6	.03
3	27.8	.02	27.8	.05
4	73.6	.06	73.6	.06

Table 4: Eigen analysis comparing frequency and damping factors of the system's flexible modes with and without the arm controllers enabled.

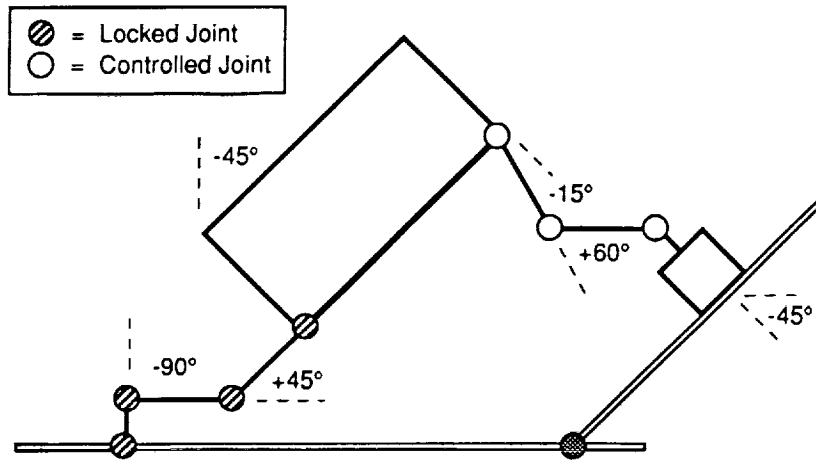


Figure 5: The geometric configuration chosen for an ORU replace task.

the complete set of possible configurations was not spanned, these values indicate how much the modes may vary. This simple analysis also showed that the dominant system frequency decreases as the distance from the worksite attach-point to the system COM increases.

### 3.2 Initial Closed-loop Analysis

To assess the effect of the position control loops, the right side of Fig. 6 shows the closed-loop transfer functions from joint command to joint angle for each controlled degree-of-freedom. Here, the nominal stiffnesses and a 1 Hz bandwidth are assumed. Some notable features of the fundamental system frequency: the dominant uncontrolled system mode remains lightly damped, lies within the control bandwidth, and is reduced by 14% to a value of 0.64 Hz (see Table 4). This reduction in frequency is due to the stiffening effect of the joint control loops on the manipulator (recall that in the open-loop transfer functions above, the manipulator joints are treated as free pinned-joints). As will be shown later, the fundamental vibration frequency decreases with increasing manipulator joint stiffness (provided by the position control bandwidth). In the limit, when the manipulator joints are infinitely stiff (rigidly locked), the manipulator/payload becomes a rigid body inertia. Moreover, the fundamental mode also decreases with increasing payload mass and inertia.

Given that the dominant system frequency is lightly damped and coupled to motion of the closed-loop manipulator, we now would like to assess degradation in the closed-loop performance. Assuming the initial pose shown in Fig. 5, a retraction maneuver is

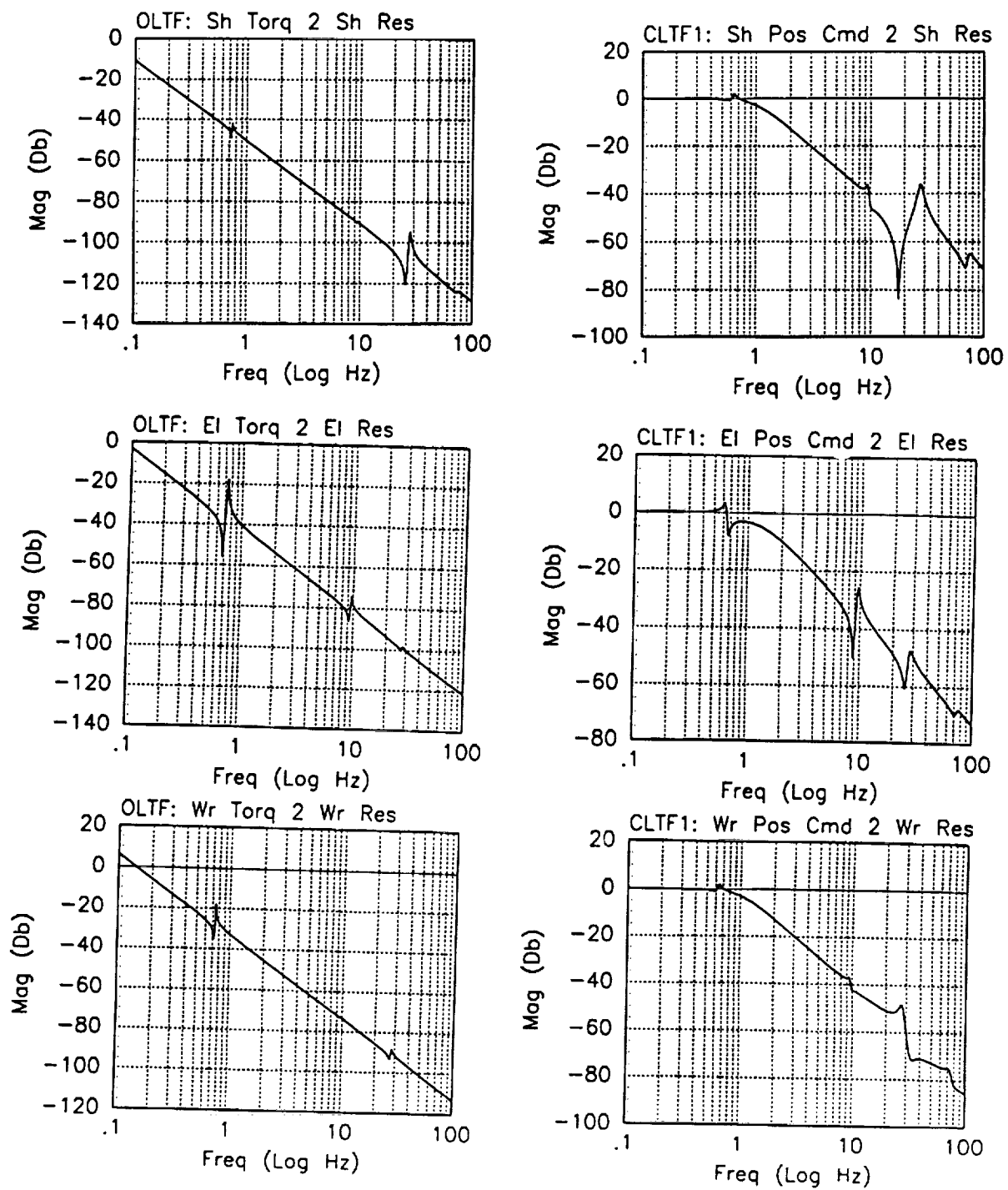


Figure 6: Open-loop (left) and closed-loop (right) transfer functions for the nominal manipulator/stabilizer system.

specified for the payload. The cartesian trajectory is a straight-line and maintains the initial orientation. The trajectory is a fifth-order spline function of time yielding a 2 ft cartesian displacement in 1 sec. Joint angle reference commands are obtained from the inverse kinematics transformation of the cartesian trajectory. This trajectory was chosen based on FTS cartesian control speed requirements, and was intended to emphasize the dynamic interactions between the arm, body, and stabilizer.

Figure 7 shows closed-loop responses of the arm and stabilizer system to the tip trajectory described above. Recall that the assumed damping coefficient for the stabilizer brake is 1%. The upper left and right plots show, respectively, time histories of 1) displacement of the manipulator/body attach-point (shoulder axis) in the Y-direction, and 2) commanded versus actual motion of the endpoint in the Y-direction. (Although not shown here, the corresponding responses in the X-direction are similar.) The lower-left time history shows the magnitude of error between commanded and actual tip trajectory while the lower right plot gives an "overhead view" of the tip (payload COM) response in inertial cartesian coordinates. As can be seen, the responses are dominated by residual vibrations of the lightly damped, uncontrolled system mode at 0.64 Hz. Although motion of the manipulator body is only  $\pm 1$  in at most, the resulting error at the endpoint takes about 33 sec to damp out to 0.03 in (throughout this analysis, 0.03 in was chosen as the endpoint settling criteria and is based on an FTS task derived requirement). Clearly, this simulation demonstrates the degradation of performance attributable to the uncontrolled motion of the compliant stabilizer. Assuming that active damping control of the ASPS itself is not an option, we now consider other alternatives to reduce residual motion of the uncontrolled mode.

### 3.3 Effects of Stabilizer Stiffness and Controller Bandwidths

One option includes structural modifications to the ASPS and WAM to increase their effective stiffness. Figure 8 plots parametric design curves showing the change in frequency and damping of the dominant uncontrolled system mode as a function of stabilizer and attach-point stiffness. These plots were done assuming the geometric pose of Fig. 5, with ASPS joints locked, arm joint control loops closed (1 Hz critically damped bandwidth), and a 25 lb payload. As might be expected, the frequency increases with  $K_{jnt}$  and  $K_{att}$ . Not as intuitive though is the effect on the uncontrolled mode's damping factor. This curve shows how the proper combination of stabilizer joint and attach-point stiffnesses can be used to significantly increase damping of the uncontrolled mode.

To get a better understanding of this phenomena, consider the option of altering the bandwidths of the arm position controllers for fixed values of  $K_{att}$  and  $K_{jnt}$ . For the same pose and payload as before, Figure 9 plots the frequency and damping of the dominant uncontrolled system mode as a function of the ratio  $f_{bw}/f_{ol}$  where  $f_{bw}$  is the joint position controller bandwidth (with critical damping assumed) and  $f_{ol}$  is the open-loop

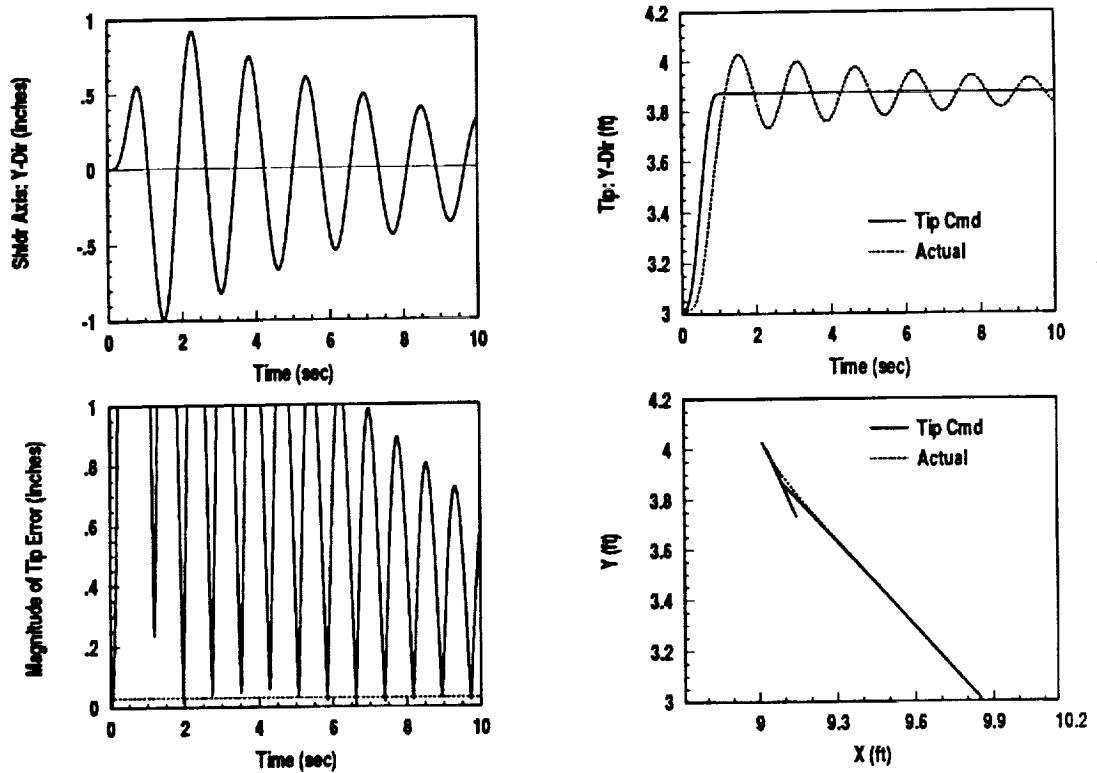


Figure 7: The system responses for the nominal configuration are dominated by the uncontrolled, lightly damped stabilizer mode.

fundamental frequency. In the upper plot, the dominant closed-loop natural frequency  $f_{cl}$  (stabilizer mode) is normalized to  $f_{ol}$ . In this plot, we confirm our previous statements that the frequency of the dominant uncontrolled mode decreases with the joint loops closed and increasing controller bandwidth. But more interesting is the behavior of the damping shown in the bottom curve — for a small range of the ratio  $f_{bw}/f_{ol} \approx [0.5, 0.8]$ , damping ratios greater than 10% can be achieved. In terms of altering the control bandwidth, one can think of the manipulator as a “tunable” spring-mass system. Considered in this manner, the closed-loop manipulator acts as vibration absorber for the flexible stabilizer system. By tuning the manipulator stiffness (position control bandwidth), stabilizer damping can be maximized. Unfortunately though, adjusting controller bandwidth to improve stabilizer damping may mean reducing the bandwidth to unacceptably low level from a closed-loop performance standpoint. For instance, for the nominal stiffnesses  $K_{att}$  and  $K_{jnt}$ , to achieve the maximum 11% damping shown in Fig. 9 would mean reducing the control bandwidth from the nominal 1 Hz to  $\approx 0.5$  Hz.

Assuming that the 1 Hz control bandwidth must be satisfied, we now show the performance improvements possible by optimizing the stabilizer and attach-point stiff-

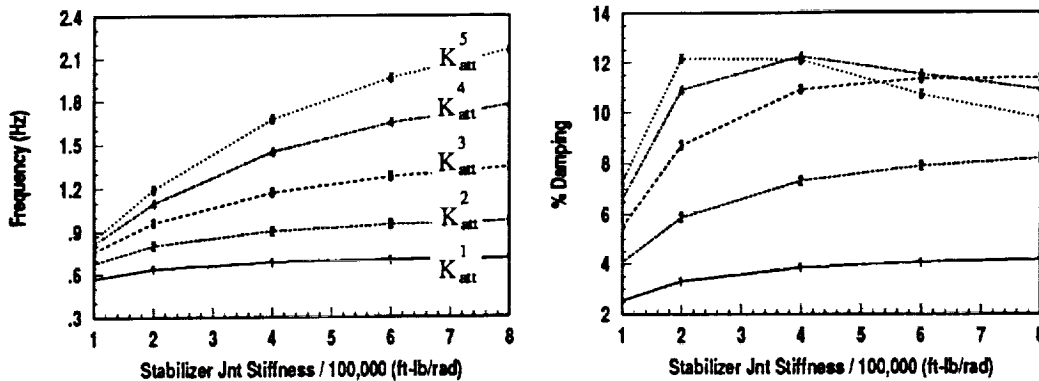


Figure 8: Frequency and damping of the dominant closed-loop stabilizer mode versus stabilizer joint stiffness for five values of the effective attach-point stiffness:  $K_{att}^1 = 40,000$   $K_{att}^2 = 80,000$   $K_{att}^3 = 160,000$   $K_{att}^4 = 320,000$   $K_{att}^5 = 640,000$   $ft-lb/rad$ .

nesses based on the design curves of Fig. 8. To achieve greater than 10% damping of the stabilizer mode, effective stiffness values of  $K_{att} = 160,000$   $ft-lb/rad$  and  $K_{jnt} = 400,000$   $ft-lb/rad$  were chosen for the attach-point and ASPS joints, respectively. Referring to Fig. 9, these values yield a ratio of  $f_{bw}/f_{ol} = 1/1.3 = 0.77$ . Using the same endpoint trajectory described above, Figure 10 shows the resulting manipulator/stabilizer responses for the "improved" design. As predicted by the design curves, damping of the stabilizer mode is significantly increased. Compared to the corresponding curves of Fig. 7, much less motion is induced at the manipulator/body attachpoint (less than  $\pm 0.3$  in) and endpoint settling time to 0.03 in is less than 5 sec. The only drawback would seem to be the minor excursion from a straight-line endpoint trajectory as shown in the lower-left cartesian response. In addition to stiffening the stabilizer output brakes, a detailed study should be done to design output brakes providing significant amounts of passive damping.

### 3.4 Residual Vibration Reduction Using Preshaping Filters for Free-space Maneuvers

In addition to stiffening stabilizer joints and the worksite attach-point, or significantly changing the manipulator control bandwidth, another method to reduce residual vibrations of the stabilizer for free-space maneuvers employs preshaping filters in the feed-forward path of the manipulator control system. The proposed command shaping technique has been developed by Singer and Seering (see [3,4,5]) and is based on the use of simple impulse sequences convolved with desired system inputs (e.g., a cartesian trajectory command). The desired system inputs are altered so that the system's natural tendency to vibrate is used to cancel residual vibration. A short time penalty (on the order of one

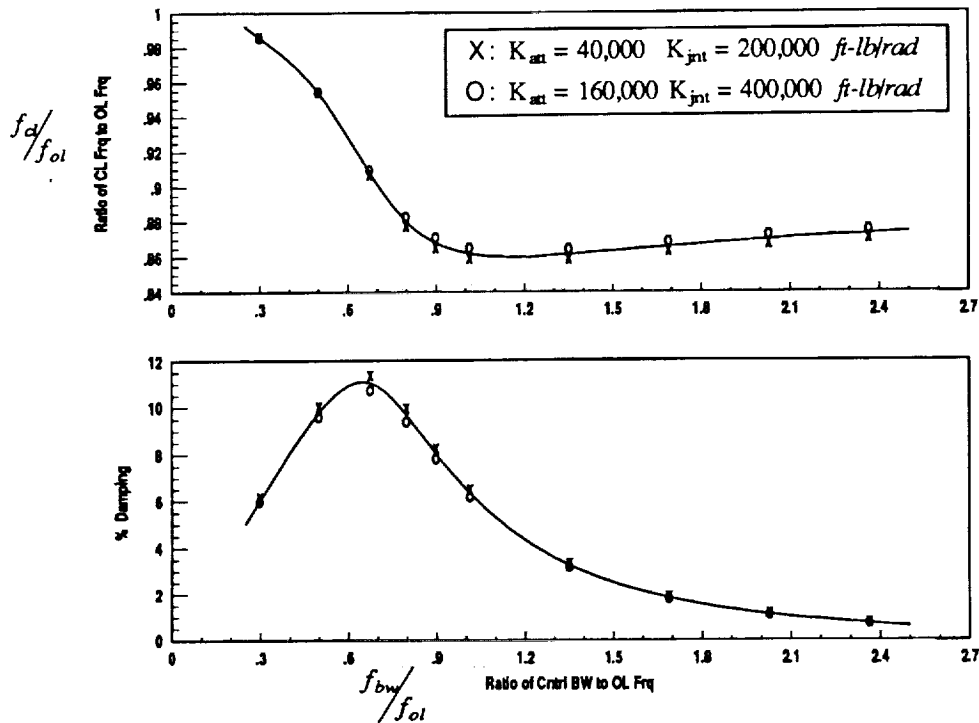


Figure 9: Frequency (normalized) and damping of the dominant closed-loop stabilizer mode versus the ratio of controller bandwidth to the dominant open-loop mode, for two sets of stabilizer and attach-point stiffnesses.

period of the primary vibration frequency) is incurred; however, the method is robust to uncertainties in the knowledge of a system's vibration frequencies (and damping factors), and can be applied to both open and closed loop systems. Moreover, the method is easy to implement and has been demonstrated in the laboratory on an in-house flexible manipulator testbed [6] as well as on the hydraulic RMS simulator at NASA Johnson Space Center [5].

Figure 11 shows how the technique is applied here to shape the cartesian reference inputs to the joint position controllers. While a full derivation and analysis of this method can be found in [3,4], design of the impulse sequence is based on the frequency and damping of the *closed-loop* system mode of concern, *i.e.*, the uncontrolled stabilizer mode. The resulting shaped commands do not contain impulses, nor do they alter the trajectory as a straight-line path. To illustrate how the inputs are changed after the convolution, a four-impulse sequence was designed for the nominal stabilizer mode ( $f_{cl} = 0.74$  Hz). Figure 12 shows the time history and cartesian trajectory before and after command shaping. As can be seen from the time history, a delay penalty is incurred ( $\Delta T \approx 2.4$  sec), but the cartesian trajectory remains a straight-line path.

Figure 13 shows the manipulator and stabilizer responses obtained using the shaped

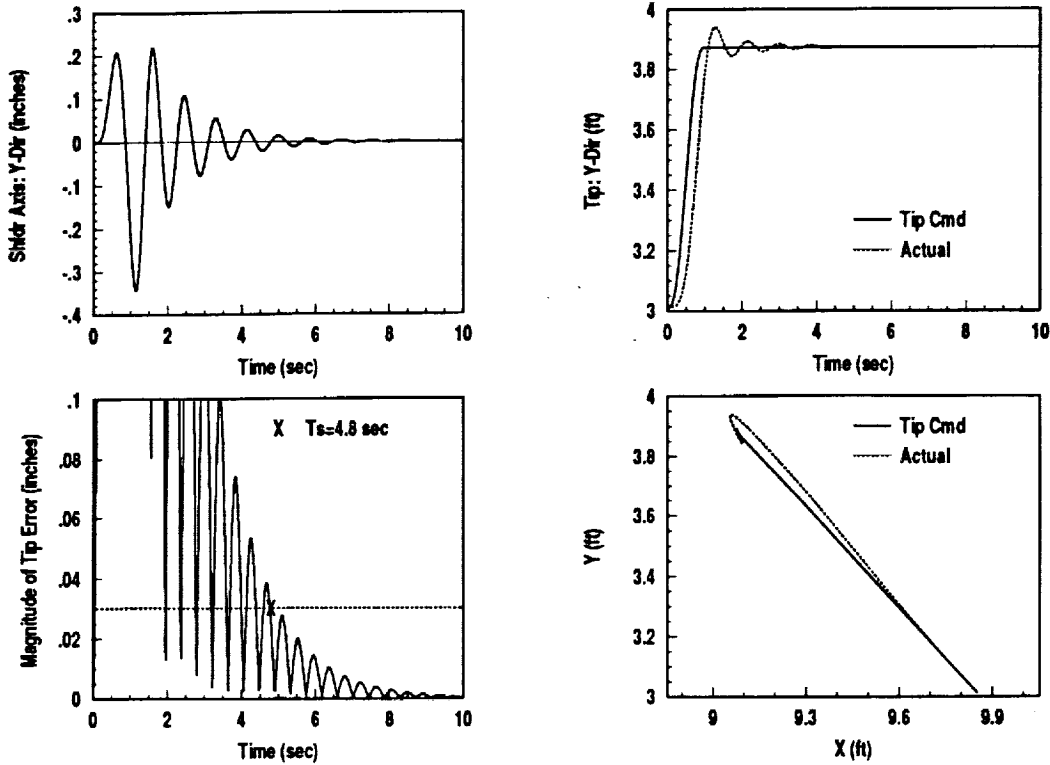


Figure 10: System response showing increased damping of the dominant stabilizer mode by using an improved combination of joint and attach-point stiffnesses

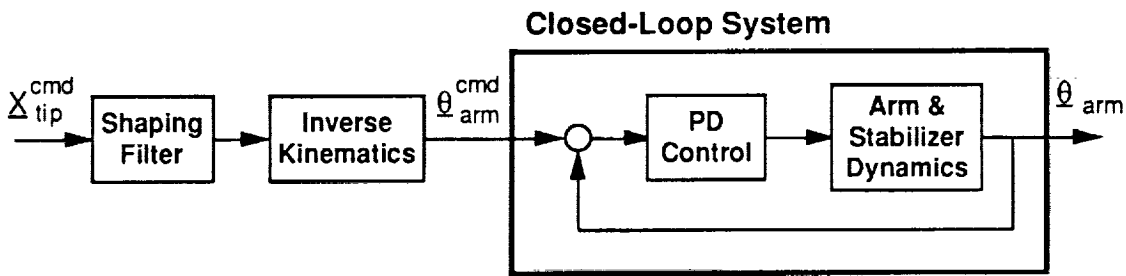


Figure 11: Block diagram showing the use of command shaping filters.

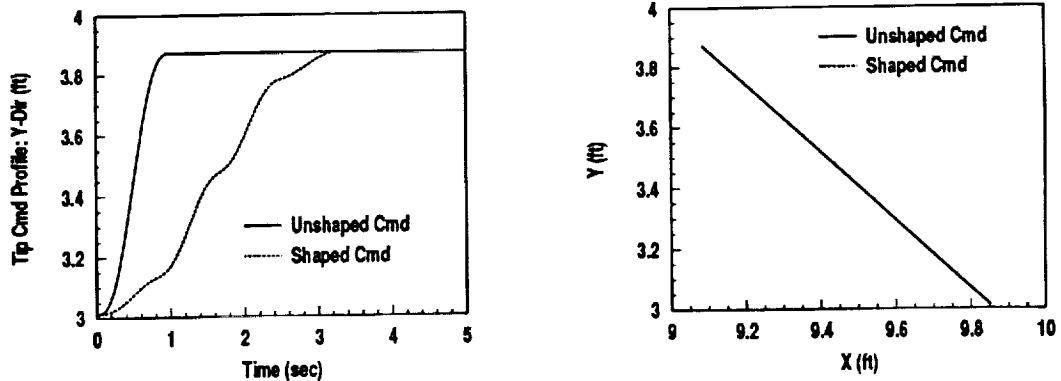


Figure 12: Effect of shaping the cartesian trajectory command with a four-impulse sequence. On the left-side plot, only the y component is shown.

cartesian trajectory above, and assuming the nominal control bandwidths and stiffnesses. Comparing the responses to the nominal case of Fig. 7, the amplitude of motion at the manipulator shoulder joint axis is reduced by a factor of ten, and the 0.03 in settling criteria is met in less than 7 sec. Also, the endpoint, while lagging the specified cartesian trajectory in time, produces less excursion from a straight-line path than seen in the previous two cases.

In the example above, the shaping filter was designed assuming perfect knowledge of the dominant vibration mode's frequency and damping ratio. This leads to the question of robustness. For instance, if a small uncertainty in the natural frequency exists, how much residual vibration will the system response induce? While robustness issues are addressed in [3,4], it can be shown that the technique is inherently insensitive to damping uncertainties. Robustness to uncertainties in the natural frequency can be improved by adding constraints in the derivation of the impulse sequence; additional constraints leads to an increased number of impulses in the sequence and also increases the delay time penalty incurred. Generally, a three- or four-impulse sequence is sufficient, with the latter being less sensitive to frequency uncertainty (in [4], analysis for an idealized system shows a four-impulse sequence to yield acceptable results for an approximate  $\pm 25\%$  error in natural frequency).

To illustrate, a second four-impulse sequence was redesigned assuming a +20% error in the nominal stabilizer mode, or  $1.20f_{cl} = 0.89 \text{ Hz}$ . As can be seen from the responses shown in Fig. 14, the technique still performs quite well despite the uncertainty. Displacement of the manipulator body is less than 0.10 in, settling time of the endpoint is less than 9 sec, and the resulting cartesian trajectory at the endpoint is very close to a straight-line path. Table 5 summarizes settling times of the four simulations discussed above. While the command shaping method demonstrates good performance for a 20% uncertainty in the dominant vibration mode, a simple adaptive scheme could be employed

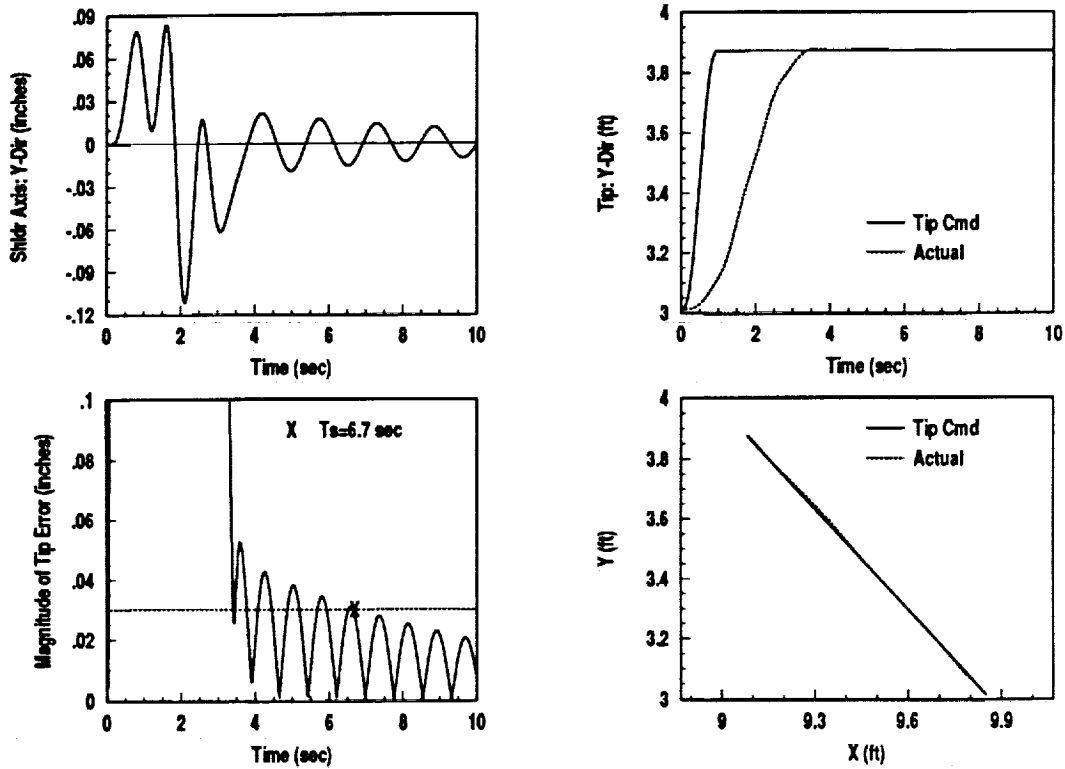


Figure 13: Using a four-impulse sequence to shape the cartesian trajectory command greatly reduces residual vibrations of the dominant stabilizer mode

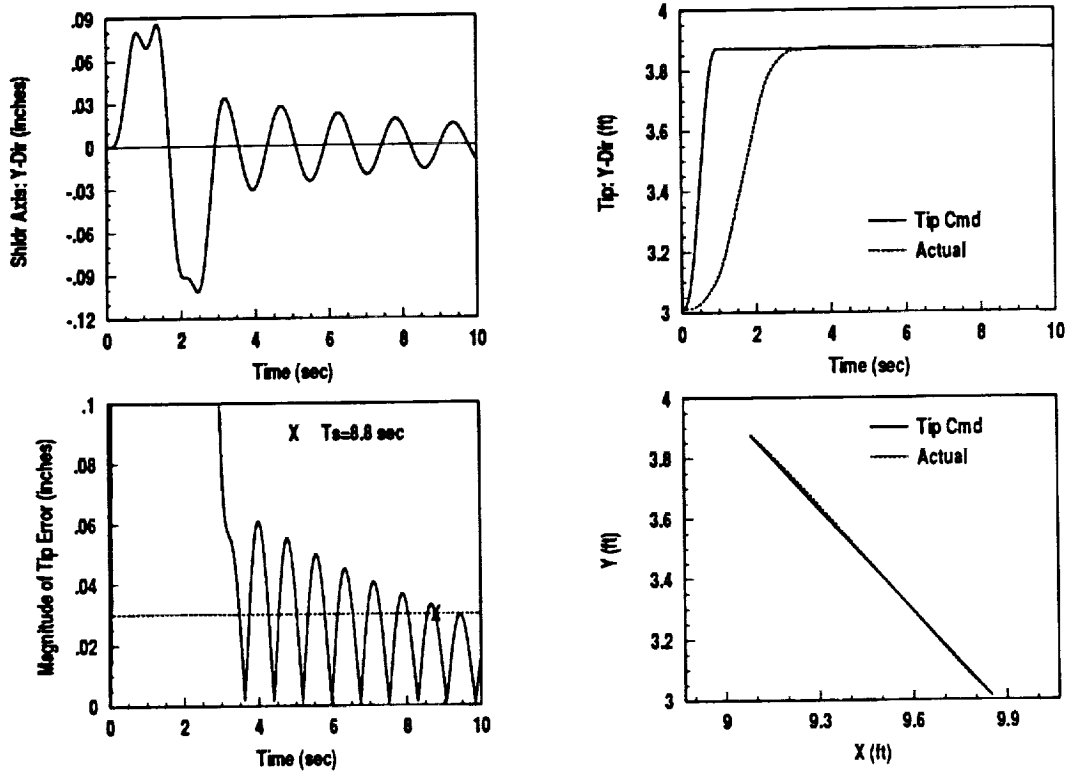


Figure 14: System response using shaping filter with 20% error demonstrates the techniques robustness to uncertainties.

Configuration	Endpoint Settling Time (sec)	Maximum Body Displacement (inch)
Nominal Stabilizer	33.0	1.0
Improved Stabilizer	4.8	0.35
Nominal Stabilizer and Shaping with No Error	6.7	0.11
Nominal Stabilizer and Shaping with 20% Error	8.8	0.11

*Table 5: Comparison of responses for the four freespace simulations*

for greater, or time-varying uncertainties. For instance, the frequency parameter of the shaping sequence could be tuned using an identification algorithm to monitor on-line the dominant system vibration frequency. Body-mounted accelerometers could be used for sensing the dominant mode.

As used here, the preshaping technique is applied to a precomputed cartesian trajectory; however, the method may be applied as well to arbitrary system inputs, such as the signals from a hand controller. Because the preshaping filters do incur a time penalty, the overall closed-loop bandwidth is effectively reduced. However, the same type of residual vibration reduction cannot be achieved by simply reducing the controller bandwidth. Moreover, reducing controller bandwidth reduces the system response to external disturbances. In the next section, we show transient responses to one type of external disturbance—a motion constraint at the endpoint. Because the shaping filters are in the feed-forward path and before the feedback loop (see Fig. 11), they do not affect (for better or worse) the response to external disturbance inputs. As such, their application is not considered in the next section.

### 3.5 ORU Extraction Simulations

One of the most common servicing tasks of FTS will include pulling objects, such as an ORU, from their worksite storage space. A concern during this process will be the interaction of the FTS and its payload with the worksite environment during and after the extraction process. During the extraction, uncontrolled motion of the compliant stabilizer/body must not lead to contact with the environment. Also, when the payload is suddenly pulled free from its holding place, during the transient response, destructive (and possibly destabilizing) impacts between the arm/payload and the worksite must be avoided. To examine these issues, the planar multi-link program described in section 2.3 was used to simulate FTS extraction of an ORU. The force control law is described in section 2.2.2. The purpose of the force control was not necessarily to develop an implementable force controller, but to simply obtain a desired endpoint force so that that body motion could be studied and to obtain initial conditions for the payload release from

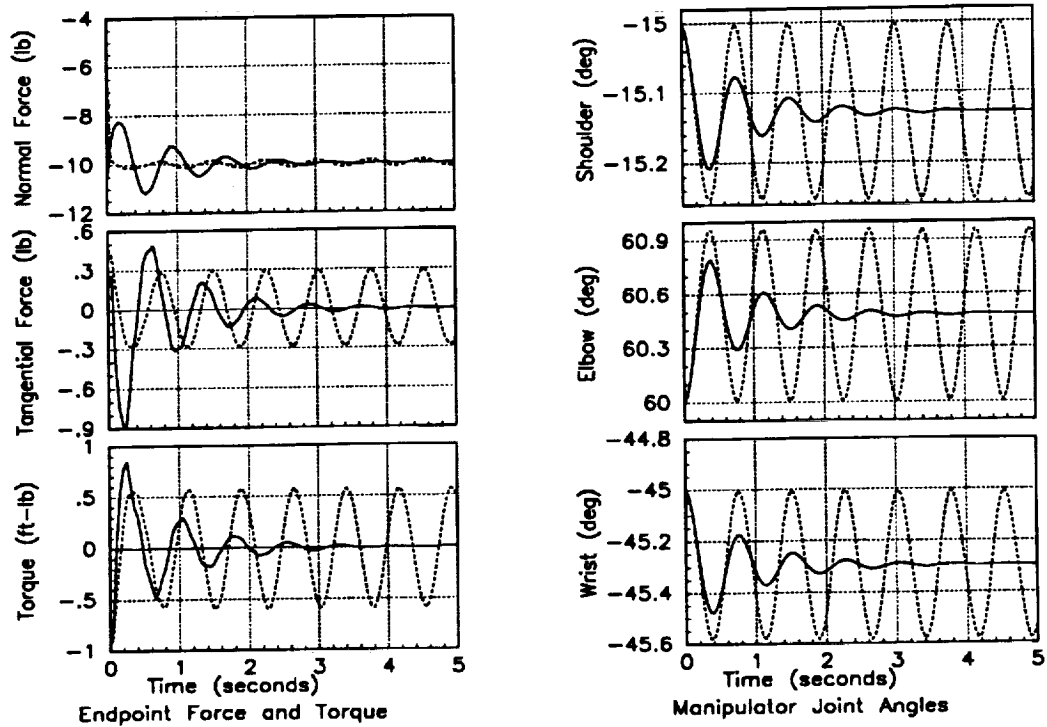


Figure 15: Endpoint force control with (solid lines) and without (dashed lines) joint rate feedback

control; recall that here we assume the ORU is rigidly grasped by the end-effector and is also rigidly fixed to the worksite. Also assumed is the initial geometry of Fig. ?? and the nominal stiffnesses  $K_{att} = 40,000$  and  $K_{jnt} = 200,000 \text{ ft-lb/rad}$ . Time histories for a 10 lb extraction force command are shown in Figure 15 with and without the use of joint rate feedback. As can be seen, the inner joint rate feedback loop considerably improves damping of the endpoint force as well as the overall stabilizer/body/manipulator motion. The final travel of the FTS body is only on the order of 0.08 in, which should be well within acceptable range for most extraction procedures.

To simulate motion of the FTS and ORU payload after the ORU has been released from the environment, the final states from the closed-loop force control on the constrained system were used as initial conditions for the unconstrained system. The nominal joint position controller described in section 2.2 was used to maintain desired payload position relative to the FTS body. Two different methods were used to command the manipulator joints upon release of the ORU from the environment. The first involved simply maintaining the joint angles at their values upon release from the environment. The second method involved commanding the joint angles such that the payload would be retracted away from the environment in a direction normal to the environment surface.

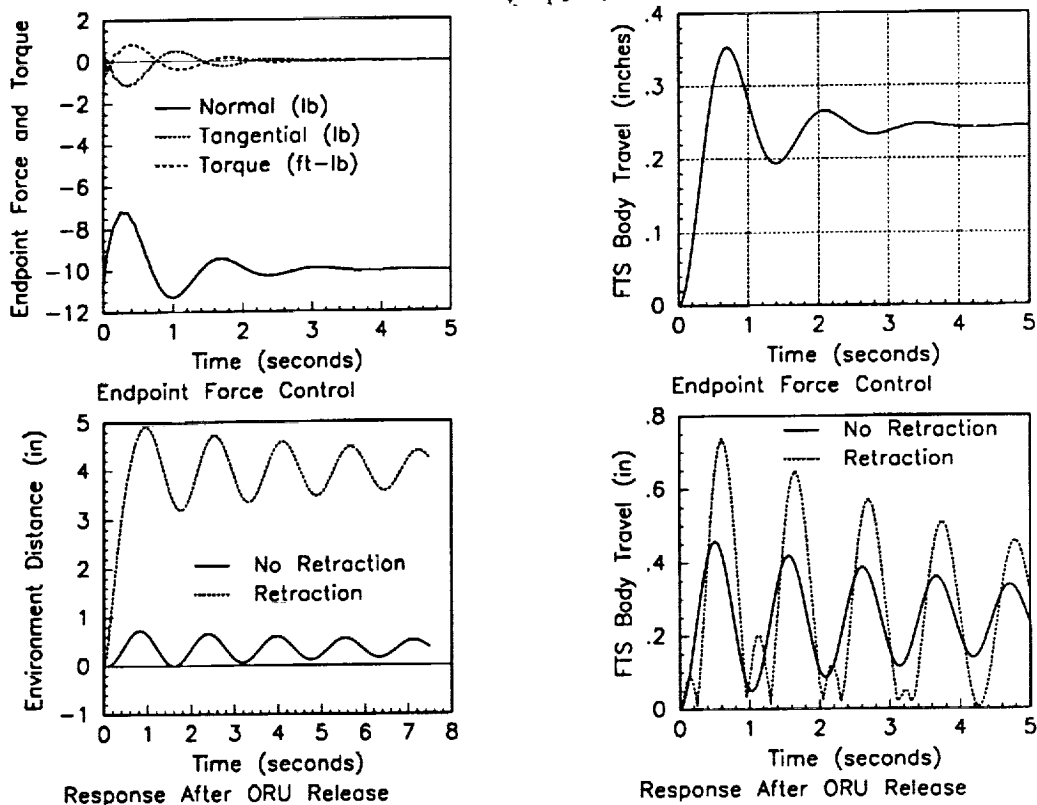


Figure 16: Simulation of 10 lb endpoint force control and ORU release from environment. The upper plots show the establishment of the 10 lb pulling force; the lower plots show the free-space motion upon release.

be retracted away from the environment approximately four inches in a direction normal to the environment surface.

Simulations of the endpoint force control and response after ORU release from the environment were conducted for 10, 25 and 50 lb extraction requirements. The results are shown in Figures 16-18, respectively. Even in the case of the 50 lb extraction command, the amount of FTS body travel was found to be less than three inches, within acceptable range for most extraction procedures. Due to the lightly damped nature of the stabilizing arm, it was found that the first method of maintaining initial manipulator angles allowed the ORU payload to impact the environment while its transient motion settled out. The second method of retracting the payload upon release showed better results, moving the ORU approximately four inches away from the environment while not significantly affecting other performance, such as FTS body travel. The two methods are compared in Figure 19 by way of endpoint position in cartesian space for the case of the 50 lb extraction command, demonstrating that the extraction method moves the payload at a 45 degree angle, or perpendicular to the environment.

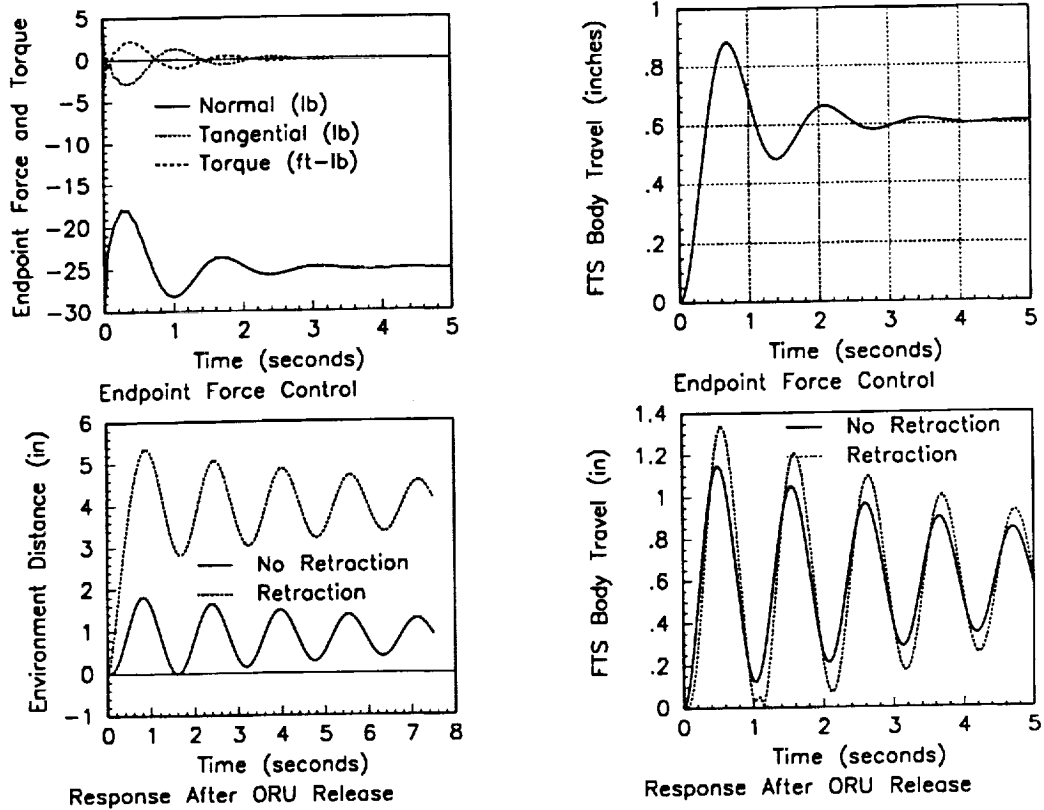


Figure 17: Simulation of 25 lb endpoint force control and ORU release from environment

No Endpoint Retraction		
Extraction Force (lb)	Settling Time (sec)	
	Nominal	Improved
10	22.06	2.3
25	28.15	3.2
50	34.38	4.2
With Endpoint Retraction		
Extraction Force (lb)	Settling Time (sec)	
	Nominal	Improved
10	29.29	3.75
25	30.65	3.85
50	34.43	4.50

Table 6: Comparison of endpoint settling times for ORU extraction simulations.

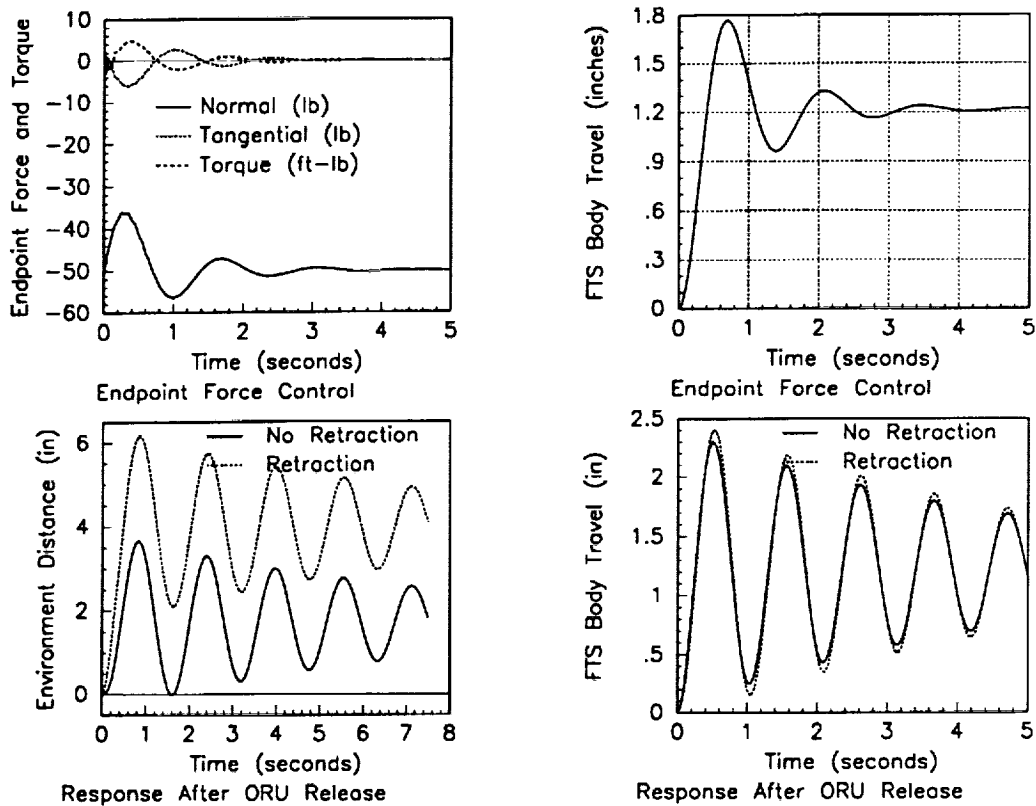


Figure 18: Simulation of 50 lb endpoint force control and ORU release from environment

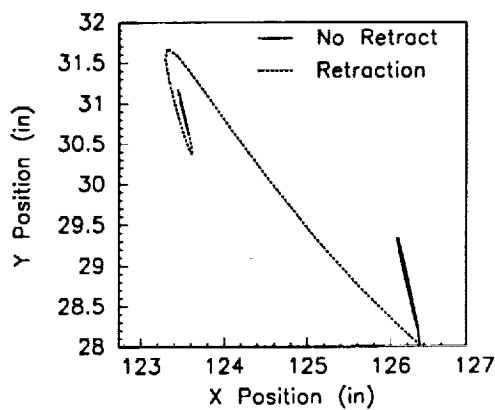


Figure 19: Comparison of endpoint position in cartesian space for the cases of retracting and not retracting the payload after release from the environment for a 50 lb endpoint force

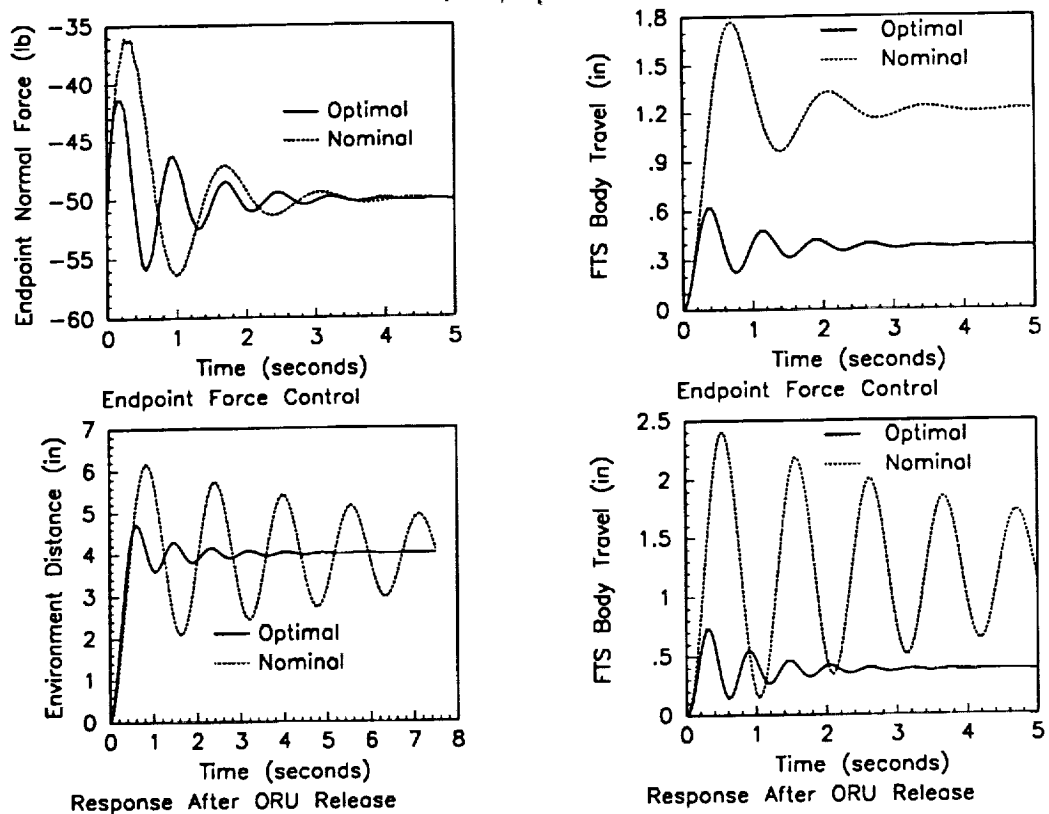


Figure 20: Comparison of nominal and improved stabilizer designs for a 50 lb extraction force

The above ORU extraction simulation was also run for the three force requirements using the “improved” stabilizer and attach-point stiffnesses describe above ( $K_{jnt} = 400,000$  and  $K_{att} = 160,000 \text{ ft-lb/rad}$ ). Results with the improved and nominal stabilizers are presented in Figure 20 for the case of a 50 lb extraction command, demonstrating that the FTS body travel with the optimal stabilizer is approximately one third of that with the nominal stabilizer. Also, as in the case of payload slewing, the payload motion damps out considerably quicker with the optimal stabilizer. Table 6 summarizes settling times for the optimal and nominal configurations after payload release for the three extraction forces with and without payload retraction.

## 4 Conclusions and Future Work

For simulation and controls analysis, a dynamic model of a flexibly stabilized manipulator has been developed. For the nominal system design considered, compliance in the braked stabilizer joints and the worksite attach-point yields a low frequency, lightly damped, dominant system mode. Frequency of the uncontrolled stabilizer mode is affected primarily by three factors:

- Mass and inertia of the manipulator payload. The frequency decreases with increasing mass/inertia.
- Geometric configuration of the stabilizer/positioner and the manipulator. The frequency decreases as the distance between the worksite attach-point and the system center-of-mass increases.
- Bandwidth of the manipulator joint position controllers. The frequency decreases as controller bandwidth increases.

Simulations illustrated the dynamic coupling between the manipulator and stabilizer system. As a result, residual vibrations of the uncontrolled stabilizer mode causes long settling times when controlling a payload at the endpoint. To reduce the residual vibrations (and thus improve performance), two means were investigated:

- Increase damping of the uncontrolled mode. Without the use of passive and/or active damping control devices, damping of the stabilizer mode was shown to be affected mostly by the frequency ratio  $f_{bw}/f_{ol}$  (position control bandwidth to frequency of the stabilizer mode in open-loop). Moderate damping levels ( $\geq 10\%$ ) can be achieved for an approximate range of  $0.5 < f_{bw}/f_{ol} < 0.8$ . For the nominal system design, this implied either a 50% reduction in control bandwidth, or stiffening the stabilizer joints and worksite attach-point by a factor of two and four, respectively. Simulating the latter, settling times were reduced nearly a factor of seven.
- Use of a command shaping technique to cancel residual vibrations. Using the nominal system configuration and shaping the cartesian trajectory commands with a four-impulse sequence, settling times were reduced by an approximate factor of five. The method performed nearly as well for a 20% uncertainty in frequency of the stabilizer mode.

To investigate interactions with the worksite environment, simulations of an ORU extraction showed the following:

- During force control of the endpoint, inner joint rate feedback loops greatly increased damping of the endpoint forces.

- When release of the ORU occurs, undesired motion of the manipulator and body is induced because of the uncontrolled stabilizer mode. While the amplitude of body motion was acceptably small, oscillations at the end-effector were significant enough to cause impact with the environment. Use of a retraction maneuver (in position control) was shown to reduce the chance of impacting the worksite.

Having shown the need to increase damping of the stabilizer mode, future work should investigate the possibility and effectiveness of incorporating passive damping elements in the ASPS braking mechanisms as well as the Worksite Attachment Mechanism. Among other issues, future work can also begin to study in greater fidelity the force control problem, such as stability and performance concerns when using an impedance control law. Also to consider is the case of an FTS arm stabilized by a RMS (or MRMS) arm. While we have already begun to develop high-fidelity simulations of an RMS, we will also have a hardware testbed capability operational in early 1991. The new testbed includes a  $20 \times 30$  ft epoxy flat floor to accommodate the following air-bearing supported systems: 1) a lightweight, flexible-link 3-DOF arm having a 15 ft reach, and 2) a self-contained free-flying vehicle featuring two smaller rigid-link arms. In addition, the proposed large space manipulator testbed [10] for NASA MSFC could also support the same type of experiments. Between the combination of these facilities, a number of space manipulator operations and configurations, such as the one depicted below, can begin to be studied and simulated in hardware.

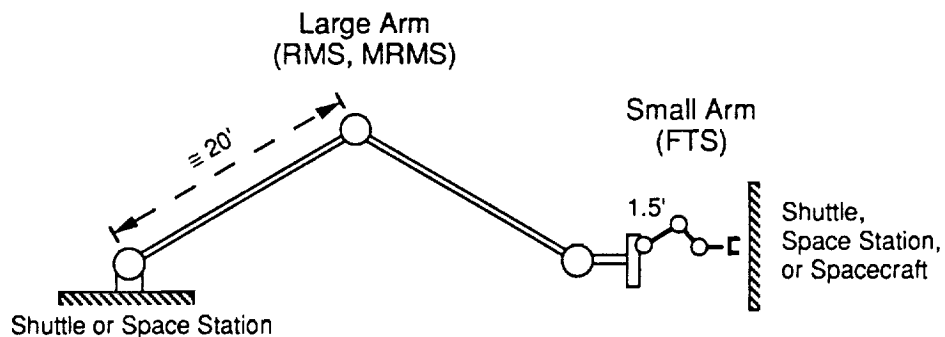


Figure 21: FTS manipulator stabilized by flexible RMS manipulator

## A Constrained Dynamics Equations for Multi-link Planar Model

Many ways exist to derive the equations of motion for a chain of rigid bodies connected in a tree topology. For this study Kane's equations [8] were used because they have been found to be the most efficient and easily implemented method. The complete derivation of the equations of motion is beyond the scope of this report, rather, the results of the derivation and the recursive implementation are presented below.

The final equations of motion for the planar multi-link rigid bodies can be presented in the form:

$$M(\theta)\ddot{\theta} = \tau + V(\theta, \dot{\theta}) \quad (1)$$

where:

$$\begin{aligned} M(\theta) &= n \times n \text{ mass matrix} \\ \theta &= \text{vector of relative joint angles} \\ &= [\theta_1, \theta_2, \dots, \theta_n]^T \\ n &= \text{number of bodies in chain} \\ \tau &= \text{vector of joint torques} \\ V(\theta, \dot{\theta}) &= \text{vector of nonlinear terms} \end{aligned}$$

The elements of the mass matrix and nonlinear vector can be expressed as:

$$\begin{aligned} M_{ij} &= \sum_{k=1}^j [m_k v_i^k \cdot v_j^k + I_k \omega_i^k \cdot \omega_j^k], \quad i, j = 1, n \\ V_i &= \sum_{k=1}^n m_k \sum_{j=1}^k v_i^k \cdot p_j^k \dot{\theta}_j^2, \quad i = 1, n \end{aligned}$$

where:

$$\begin{aligned} m_k &= \text{mass of the } k\text{th body} \\ v_i^k &= \text{the } i\text{th partial velocity of the c.g. of the } k\text{th body} \\ I_k &= \text{the mass moment of inertia of the } k\text{th body about its c.g.} \\ p_j^k &= -C_j r_j^{cg} \text{ for } j = k \\ &= -C_j r_j^l \text{ for } j \neq k \\ C_j &= \text{the direction cosine matrix relating body } j \text{ to the inertial frame} \\ r_j^{cg} &= \text{position of } j\text{th c.g. relative to body } j \text{ attach point in body } j \text{ frame} \\ r_j^l &= \text{position of body } j+1 \text{ attach point in body } j \text{ frame} \end{aligned}$$

The above equations describe the unconstrained planar motion of  $n$  links with  $n$  rotational degrees of freedom. Several methods exist for adding constraints to the links such that the links will have  $n - p$  DOF, where  $p$  is the number of constraints. The method used here was to employ Lagrange multipliers, which have the advantage of yielding the endpoint forces and torques while simultaneously constraining the system. A holonomic (position dependent) constraint on the system can be expressed in the form:

$$\Phi = [\phi_1(\theta), \phi_2(\theta), \dots, \phi_p(\theta)]^T = Q$$

For the case of constraining the endpoint in translation and rotation the three constraint equations would involve the inertial  $x$  and  $y$  position of the endpoint of the  $n$ th body and its inertial angle. Taking the derivative of  $\Phi$  with respect to time yields the constraint Jacobian matrix,  $B$ :

$$\frac{d}{dt}\Phi = \left[ \frac{\partial}{\partial \underline{\dot{q}}} \Phi \right] \underline{\dot{q}} = B \underline{\dot{q}} = 0$$

The time derivative of the above equation yields the constraint equation:

$$B \ddot{\underline{q}} = -\dot{B} \underline{\dot{q}} \quad (2)$$

This equation can then be used in conjunction with the unconstrained equations and Lagrange multipliers,  $\lambda$ , to get the final form for the constrained system [9]:

$$\begin{bmatrix} M & B^T \\ B & 0 \end{bmatrix} \begin{Bmatrix} \ddot{\underline{q}} \\ \lambda \end{Bmatrix} = \begin{Bmatrix} \underline{\tau} + \underline{V} \\ -\dot{B} \underline{\dot{q}} \end{Bmatrix}$$

In order to demonstrate the relationship between  $\lambda$  and the endpoint forces, the equations for an unconstrained system with inertial  $F_x$  and  $F_y$  endpoint forces and  $T_\phi$  endpoint torque (see Figure 22) are presented below:

$$M \ddot{\underline{q}} = \underline{\tau} + \underline{V} - G \begin{Bmatrix} F_x \\ F_y \\ T_\phi \end{Bmatrix} \quad (3)$$

where:

$$G = B^T \quad (4)$$

and therefore:

$$\lambda = \begin{Bmatrix} F_x \\ F_y \\ T_\phi \end{Bmatrix} \quad (5)$$

The joint accelerations and endpoint forces and torques can then be determined from:

$$\begin{Bmatrix} \ddot{\underline{q}} \\ \lambda \end{Bmatrix} = \begin{bmatrix} M & B^T \\ B & 0 \end{bmatrix}^{-1} \begin{Bmatrix} \underline{\tau} + \underline{V} \\ -\dot{B} \underline{\dot{q}} \end{Bmatrix}$$

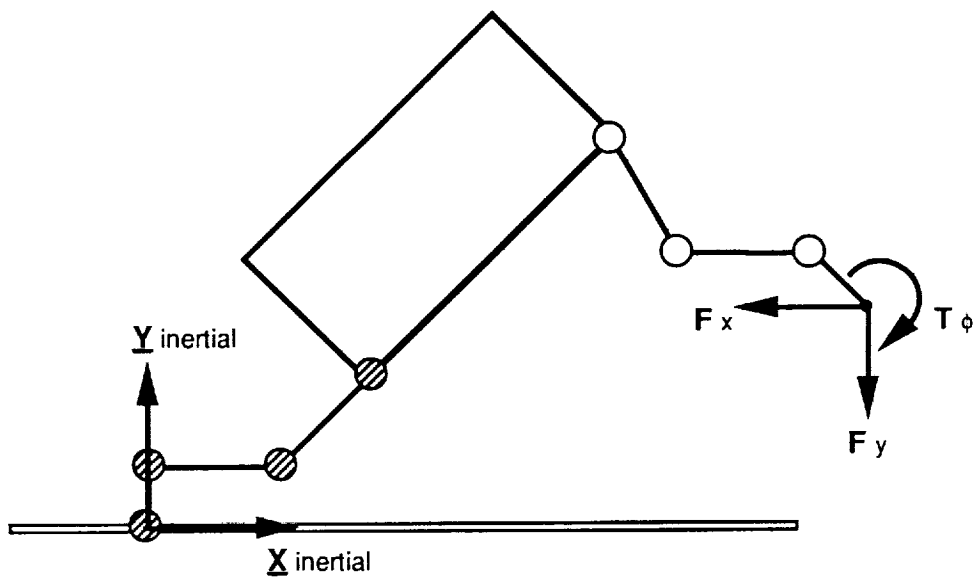


Figure 22: Endpoint Inertial Forces and Torques

## References

- [1] *FTS Phase B Trade Study Final Report*, Martin Marietta Astronautics Group, Denver, CO, Vol. II, pg. 1-1-4, July 1988.
- [2] *FTS Design Criteria Document*, Martin Marietta Astronautics Group, Denver, CO, Rev. N, pg. 416, March 1990.
- [3] Singer, N.C., "Residual Vibration Reduction in Computer Controlled Machines," Ph.D. dissertation, Artificial Intelligence Laboratory, M.I.T., February 1989.
- [4] Singer, N.C., and Seering, W.P., "Preshaping Command Inputs to Reduce System Vibration," A.I. Memo No. 1027, The Artificial Intelligence Laboratory, M.I.T., May 1988.
- [5] Singer, N.C., and Seering, W.P., "Experimental Verification of Command Shaping Methods for Controlling Residual Vibration in Flexible Robots," *Proceedings of the 1989 American Control Conference*, May 23-25, 1990, San Diego, California, pp 1738-1744.
- [6] Ramey, M.F., "Seering's Method of Residual Vibration Reduction Applied to the Manipulation of a Flexible Payload," Robotics Group Memo, Research & Technology Dept., Martin Marietta Space Systems Company, Denver, CO, September 1990.
- [7] Integrated Systems, Inc., 2500 Mission College Blvd., Santa Clara, CA, 95054, *MATRIXx<sup>TM</sup> User's Guide*, 1990.
- [8] Kane, T.R., and Levinson, D.A., "Dynamics: Theory and Applications," McGraw-Hill Book Company, 1985.
- [9] Shabana, A. A., "Dynamics of Multibody Systems," John Wiley and Sons, 1989.
- [10] *Informal Proposal to NASA-MSFC for a Space Manipulator Testbed*, R&T Robotics Group, Martin Marietta Space Systems Company, Denver, Colorado, December 1990.

111

Faint, illegible text at the bottom of the page, possibly bleed-through from the reverse side.